

Effect of plasma actuator control parameters on a transitional flow

Arnob Das Gupta[✉] and Subrata Roy[✉]

Applied Physics Research Group, Department of Mechanical and Aerospace Engineering, University of Florida, Gainesville, FL 32611, United States of America

E-mail: arnobdgupta@ufl.edu and roy@ufl.edu

Received 22 October 2017, revised 24 January 2018

Accepted for publication 16 February 2018

Published 7 March 2018



CrossMark

Abstract

This study uses a wall-resolved implicit large eddy simulation to investigate the effects of different surface dielectric barrier discharge actuator parameters such as the geometry of the electrodes, frequency, amplitude of actuation and thermal effect. The actuator is used as a tripping device on a zero-pressure gradient laminar boundary layer flow. It is shown that the standard linear actuator creates structures like the Tollmien–Schlichting wave transition. The circular serpentine, square serpentine and spanwise actuators have subharmonic sinusoidal streak breakdown and behave like oblique wave transition scenario. The spanwise and square actuators cause comparably faster transition to turbulence. The square actuator adds energy into the higher spanwise wavenumber modes resulting in a faster transition compared to the circular actuator. When the Strouhal number of actuation is varied, the transition does not occur for a value below 0.292. Higher frequencies with same amplitude of actuation lead to faster transition. Small changes (<4%) in the amplitude of actuation can have a significant impact on the transition location which suggests that an optimal combination of frequency and amplitude exists for highest control authority. The thermal bumps approximating the actuator heating only shows localized effects on the later stages of transition for temperatures up to 373 K and can be ignored for standard actuators operating in subsonic regimes.

Keywords: plasma actuator, transition to turbulence, frequency, voltage, geometry, serpentine, oblique wave

(Some figures may appear in colour only in the online journal)

1. Introduction

Plasma actuators have increased in prevalence as active flow control device over last three decades [1]. In general, plasma actuators can be classified into three main categories based on their discharge characteristics [2]. These are dark discharge, glow discharge, and arc discharge. This study focusses on actuators based on glow discharge. The most frequently used glow discharge plasma actuators are the surface dielectric barrier discharge (SDBD) actuators. The commonly used design of an SDBD actuator is depicted in figure 1 where the plasma is formed along the line of actuation. SDBD actuators are usually powered with a high voltage (~kV) sinusoidal alternating current (~kHz). The electric field generated ionizes the gas surrounding the exposed electrode and creates plasma discharge. The asymmetrically placed electrodes cause the electric field

to induce an electrohydrodynamic body force directed normal to the line of actuation (see figure 1). This force finally creates a wall jet via collisional mechanism and allows flow manipulation in the vicinity of the plasma actuator.

Depending on the input signal waveform or geometry of the electrodes, all SDBD actuators can be categorized as standard linear SDBD actuators [3, 4], nanosecond pulsed discharge (NPD) actuators [5, 6], sliding discharge actuators [7, 8], serpentine plasma actuator [9–14] and plasma synthetic jet actuators [15, 16]. Numerical and experimental studies have shown SDBD plasma actuators can be used to either suppress [17–20] or enhance [21, 22] the growth of Tollmien–Schlichting (TS) waves and thereby delaying or advancing the transition to turbulence. Altering the geometry or orientation of the electrodes can provide additional control authority over the flow [10, 11, 16, 23]. Recently, Dorr and Kloker [24] used plasma actuators

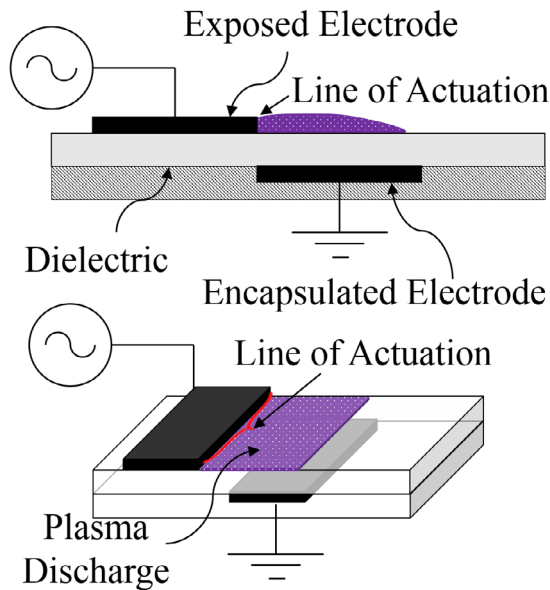


Figure 1. Schematic of a standard SDBD plasma actuator depicting the electrode configuration and plasma formation along the line of actuation of the exposed electrode.

to delay crossflow transition. Jousset *et al* [14] studied a serrated (triangular shape) electrode configuration under quiescent flow conditions. This actuator created strong filamentary discharges at the tip of the exposed electrode. This allowed the actuator to generate higher local streamwise velocity than the standard linear actuator for the same input signal. Wang *et al* [12] also studied a similar sawtooth DBD plasma actuators to control flow separation over a stalled NACA 0015 airfoil. They found that for similar power consumption the delay in stall angle achieved by a sawtooth is higher in comparison to the standard linear SDBD actuator. They concluded that this was a combined effect of the higher velocity at the tip of the actuator and the near wall vortices in the troughs. Gupta and Roy [13] studied the fundamental transition mechanism using a square serpentine plasma actuator. It was shown that the square serpentine plasma actuators undergo oblique wave transition which allows a faster transition in comparison to other secondary instability transition scenarios for the same perturbation amplitude. The same case is compared here with other actuator designs and the simulation details are provided in section 2.

Besides the geometry and orientation of the SDBD actuator, frequency and amplitude of actuation are also important in controlling transitional flow. Huang *et al* [25] showed that lower duty cycle input signal performs similar to a higher duty cycle signal in controlling separation over a turbine blade, which in turn saves electrical power input. Visbal *et al* [26] numerically showed that unsteady plasma forcing provides better flow separation control than a steady forcing. Similar work on separation control was recently performed experimentally [27], providing the importance of frequency of actuation. Bénard *et al* [28] studied a wide range of frequencies to demonstrate its impact on a fully turbulent boundary layer. However, some studies [20, 24] ignore the impact of frequency of actuation on the base flow, assuming that the

frequency of actuation is orders of magnitude higher than the base flow instability frequencies.

The amplitude of actuation, which is related to the voltage at which the actuator operates, has a significant impact on the background flow field. The amplitude can also be related to the ratio of the maximum mean plasma jet velocity magnitude to the freestream velocity of the background flow field. However, for a flow control to be efficient, an optimal amplitude of actuation should be used so that excess power is not dumped into the system. Riherd and Roy [20] numerically studied different amplitudes of actuation and showed that for smaller amplitudes, plasma actuators provide optimal perturbations, while higher amplitudes lead to non-linear effects and do not resemble boundary layer streaks [29, 30]. Roy *et al* [31] presented the combined impact of geometry, frequency, and amplitude of plasma actuation in controlling drag due to flow separation behind a model truck.

The current study numerically investigates the impact of geometry, frequency, and amplitude of plasma actuation as a tripping device on a zero-pressure gradient laminar boundary layer flow over a flat plate by approximating the actuator as a distributed forcing function. This study provides an extension to the previous work [13] where a square serpentine actuator was numerically investigated to understand the transition mechanism. A wall resolved implicit large eddy simulation (ILES) is conducted to investigate the effect of plasma actuation as a tripping mechanism to generate fully developed turbulent flow field. This study provides information on what the optimal design of the actuators should be to promote the transition to turbulence. A faster transition would imply that the flow gets turbulent faster for similar input perturbation energy and thus can be more efficient for flow mixing and control turbulent flow separation [11, 26]. Promoting transition to turbulence helps in controlling flow separation by breaking down larger vortical structures into smaller structures, thereby entraining more fluid to the separation region. Visbal *et al* [26] have presented control of flow separation by advancing transition to turbulence using plasma actuators for a flow around NACA 0015 airfoil, ramp and a wall-mounted hump. The current study also provides a knowhow on the similarity between the flow structures and transition mechanism among the different serpentine plasma actuators as observed in quiescent conditions [10]. The impact of steady and unsteady actuation by using a steady body force and an unsteady body force is also explored. The amplitude of plasma actuation is varied (5%–14% of freestream velocity) to achieve a controlled bypass transition [29].

It is known that the dielectric surface of the SDBD actuators gets heated up [31–33]. Temperatures have been shown to reach up to 573 K for some dielectrics [33]. A lot of factors impact the surface temperature including operating voltage, frequency, and dielectric material. IR measurements on serpentine actuators showed temperatures of around 323 K at locations where the radius of curvature of the electrode is small causing the formation of strong filamentary discharges and an increase in local plasma body force [31]. Therefore, the impact of thermal heating by the actuator on transition is also investigated.

This paper is structured as follows. Section 2 gives a brief description of the numerical approach taken to study the problems, section 3 discusses the results for different cases studied and finally, conclusions are drawn in section 4.

2. Computational approach

2.1. Numerical method details

The unfiltered compressible Navier–Stokes equations were solved using modal discontinuous Galerkin method without incorporating any turbulence modeling. The simulations were carried out in an in-house multiscale ionized gas (MIG) flow code. Legendre polynomials were used as interpolating functions for solutions inside the discontinuous elements. The spatial discretization was done using a third order accurate scheme ($P = 2$) and two-step fully explicit Runge Kutta method was used for the temporal terms. Gauss–Legendre quadrature rules were used for numerical integration with $P + 3$ integration points in each direction. The local Lax–Friedrichs flux was used for the convective numerical flux and local discontinuous Galerkin method was used for the viscous numerical fluxes. For all the cases, the non-dimensional time step was $\Delta t^+ = u_{\tau,i}^2 \Delta t / \nu = 0.0048$, where $u_{\tau,i}$ is the inlet friction velocity and ν is the kinematic viscosity. The non-dimensional time step is below the minimum wall scaled Kolmogorov timescale of $\tau_{\eta}^+ = u_{\tau,i}^4 / \varepsilon \nu = 0.02$ (ε is the dissipation rate per unit mass) in the turbulent region and is considered adequate for the flow simulations [34]. The flow was allowed to convect two times ($3100\nu/u_{\tau,i}^2$) over the entire streamwise length before the mean flow calculations were started. The mean flow calculations were carried out over a period of $1600\nu/u_{\tau,i}^2$.

The freestream Mach number was set to 0.5 (165.61 m s^{-1}). The freestream static pressure P_{∞} was 10 132.5 Pa and the static temperature T_{∞} was 273 K. A Blasius profile corresponding to Reynolds number based on streamwise location $\text{Re}_x = 3.75 \times 10^5$ was used at the inlet and the domain extends from $\text{Re}_x = 3.75 \times 10^5$ to 8×10^5 ($\text{Re}_{\theta} = 400$ to 1100). This range of Reynolds number falls within the range studied in previous literature [35, 36] for transition to turbulence in a zero-pressure gradient boundary layer flow. It should be noted that Mach 0.5 was chosen since higher freestream velocity provided smaller computational time for similar mesh parameters. At Mach 0.5, the density variations were found to be low enough ($<2\%$) that compressibility can be ignored. Therefore, we could still compare our work with incompressible cases (requires longer computational time) and the higher velocity reduced our computational time. The wall was kept at no slip adiabatic conditions. Both top and outlet boundary conditions were obtained by linear extrapolation. The domain was periodic in the spanwise direction.

2.2. Actuator forcing mechanism

The laminar base flow was tripped using a modified version of the first-principles body force model [11, 13, 37]. This model was used to simulate the plasma actuator forcing and is given by equation (1).

$$\begin{aligned} F_{\zeta} &= \frac{F_{\zeta_0}}{\sqrt{F_{\zeta_0}^2 + F_{y_0}^2}} \exp \left\{ - \left[\frac{(\zeta - \zeta_0) - (y - y_0)}{y - y_0 + y_b} \right]^2 - \beta_{\zeta} (y - y_0)^2 \right\} A |\sin(\omega_0 t)| \\ F_y &= \frac{F_{y_0}}{\sqrt{F_{\zeta_0}^2 + F_{y_0}^2}} \exp \left\{ - \left[\frac{(\zeta - \zeta_0)}{y - y_0 + y_b} \right]^2 - \beta_y (y - y_0)^2 \right\} A |\sin(\omega_0 t)|. \end{aligned} \quad (1)$$

In equation (1), $F_{\zeta_0} = 2.6$, $F_{y_0} = 2.0$, $\beta_{\zeta} = 1.44 \times 10^6$, $\beta_y = 1.8 \times 10^6$ and $y_b = 6.65 \times 10^{-4}$. The last three parameters provide the extent of the exponential distribution and are scaled such that the body force decays by 99% within $\delta_i/4$ where δ_i is the inlet boundary layer thickness. The amplitude of perturbation A relates to the fourth power of voltage [37] applied across the SDBD actuator. The actuator location ζ_0 and y_0 are varied for different cases. The location of the actuation is given by ζ_0 and y_0 which correspond to the points along the line of actuation. The force F_{ζ} is always directed normal to the line of actuation (ref. figure 1), while the force F_y is always directed in negative wall-normal direction. The amplitude of perturbation is set such that the velocity ratio $\gamma = u_p/U_{\infty}$ takes a range of values, where u_p is the maximum mean velocity magnitude generated by the actuator in quiescent conditions and U_{∞} is the freestream velocity. The velocity ratio and amplitude A are related as $\gamma = 2.1093 \times 10^{-4} A^{0.6314}$ [13]. Since the plasma actuator generates random streamers, a random amplitude is added to the actuator forcing to make it non-uniform along the line of actuation. This is also done to remove symmetries in the spanwise direction when the flow becomes turbulent. A pseudo-random number r which varies from $-0.1A$ to $0.1A$ was added to the amplitude A in equation (1). The actuator center location is at a distance $4\delta_i \approx 36\delta_i^*$ from the inlet, where δ_i^* is the inlet displacement thickness. This location is almost four times the one chosen by Schlatter and Örlü [38] and corresponds to $\text{Re}_x = 4.13 \times 10^5$ ($\text{Re}_{\theta} = 430$). Although the location of actuation (tripping) has a large impact on the flow [38], the variation of this parameter has not been investigated for the present study.

The 3D forcing (except for the linear actuator) due to the serpentine actuator geometry creates two kinds of regions, namely the pinching region (center z -plane), where the force vectors (F_{ζ}) are directed towards each other and the spreading region (spanwise boundary planes) where the forces are directed away from each other. The combined effect of pinching and spreading creates 3D vortical structures [10] which are beneficial in flow control applications.

2.3. Mesh details

The streamwise (x -direction), wall-normal (y -direction) and spanwise (z -direction) domain sizes correspond to $400\delta_i^*$, $59\delta_i^*$ and $15\delta_i^*$ respectively. The mesh is uniform in the streamwise and spanwise direction and it is stretched in the wall-normal direction. The outlet boundary elements are stretched to avoid reflections. The flow is relaminarized in the stretched outlet region using a sink term, similar to a sponge region [39]. All the variables scaled with wall parameters (also called wall-scaled) have a superscript of ‘+’ and are defined using local friction velocity u_{τ} and kinematic viscosity ν . The lower-case variables denote instantaneous data and the lower case primed

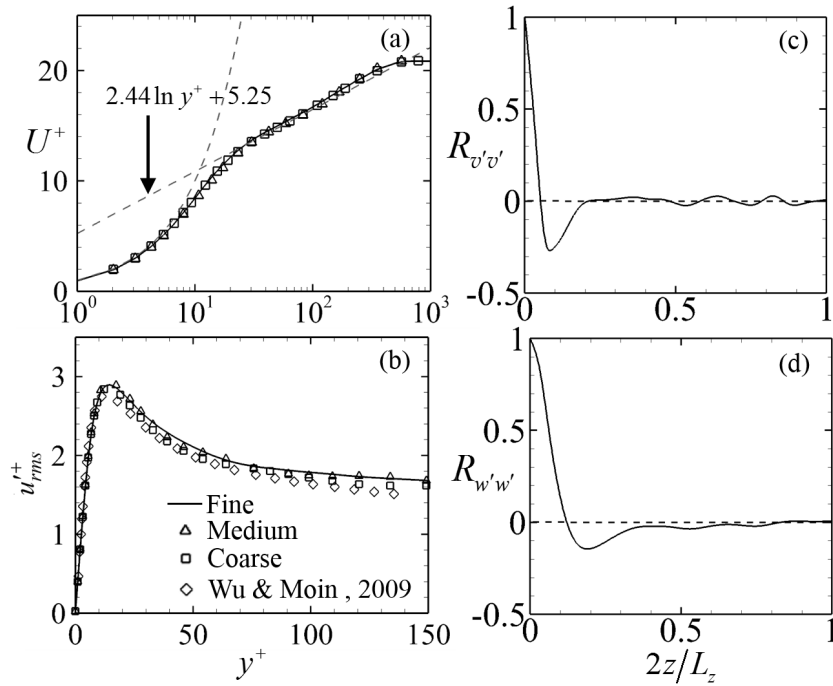


Figure 2. Mesh comparison of turbulent mean statistics at $Re_\theta = 1000$ with DNS results [35] at $Re_\theta = 900$ for (a) mean velocity profile and (b) streamwise RMS fluctuations along the wall normal direction. Two-point correlation for the fine mesh at $Re_\theta = 1000$ and $y^+ = 10$ for (c) wall-normal, (d) spanwise RMS fluctuations in the spanwise direction.

variables denote instantaneous fluctuations. The parameters with subscript ‘rms’ denote root mean square (RMS) value, where the averaging is done in time and spanwise direction. The variables with an overhead bar denote ensemble average over time and spanwise direction.

The mesh size of $750 \times 64 \times 64$ was chosen after a grid resolution study was performed for a square serpentine actuator ($\gamma = 0.1, \omega_0 = 1000$ Hz) using mesh sizes of $750 \times 48 \times 32$ (coarse), $750 \times 64 \times 32$ (medium), and $750 \times 64 \times 64$ (fine). All mesh sizes have the first grid point y_{wall}^+ ranging from 0.45 (inlet) to 1.04 (outlet) which corresponds to $y = 1.7 \times 10^{-5}$ m. Variation of mean and fluctuating velocity profiles due to mesh is shown in figure 2 along with the variation of two-point correlations of spanwise and wall-normal fluctuations in spanwise directions at $Re_\theta = 1000$. This is an approximate location where the flow becomes fully turbulent. The present results are compared to DNS results of Wu and Moin [35] at $Re_\theta = 900$. The mean velocity profile shows no significant variation due to mesh size. The medium and fine mesh show similar results for the streamwise RMS fluctuation u_{rms}^+ indicating the fine mesh is adequate for the present study. The two-point correlation for the fine mesh shows that the fluctuations decorrelate within a quarter of the spanwise domain length ($2z/L_z = 0.5$). This indicates that the domain is sufficient for the current simulations.

3. Results

3.1. Effect of actuator geometry

Four different geometries of the actuator electrode were tested. These include the standard linear SDBD, circular serpentine, spanwise array and square serpentine plasma actuator. From

here on, these actuators will be called linear, circular, spanwise and square actuators respectively. For the numerical study, the plasma body force mentioned in section 2.2 is applied along the line of actuation provided in figure 3. The spanwise and streamwise extent of the actuators is denoted as λ . This wavelength is also equal to the spanwise domain length and determines the shape of a particular serpentine actuator. While the wavelength has an impact on flow control applications [11], for the present study it was not varied. The arrows depicted in figures 3(a)–(d) are the directions of the force F_ζ which are always normal to the line of actuation. Due to the 2D nature of the serpentine and spanwise actuators, F_ζ is decomposed into two components, namely the streamwise, F_x and spanwise, F_z component. It should be noted that the linear actuator only has the streamwise component. For the present study, γ is chosen to be 0.1 and $\omega_0 = 1$ kHz. It should be noted that u_p due to this forcing is around 16.5 m s^{-1} (rms fluctuations = 11.6 m s^{-1}) while the current state of the art actuators can generate utmost 11 m s^{-1} [40]. For the same velocity ratio and different freestream velocity, Gupta and Roy [13] showed that the flow transitions almost identically. Therefore, the conclusions from this paper can be applied to lower freestream velocity ($<100 \text{ m s}^{-1}$) cases for which the required u_p would be less than 11 m s^{-1} .

The flow does not transition to a fully developed turbulent profile for the linear and circular actuator cases in the chosen domain. This can be observed in the normalized streamwise velocity streaklines shown in figure 4. The spanwise and square actuator cases show fully developed turbulence at a downstream location. The linear actuator creates 2D waves similar to the TS wave transition [41]. However, the circular, spanwise, and square actuators generate wavy streak pattern similar to a subharmonic sinuous mode observed in oblique

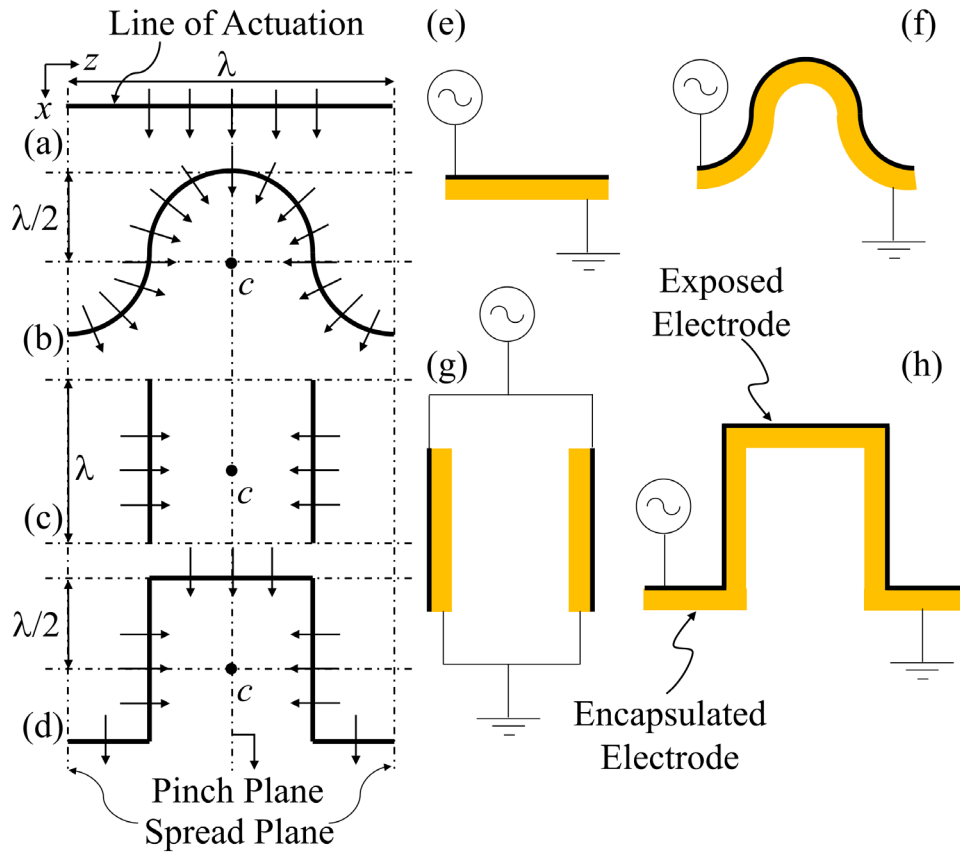


Figure 3. Schematic of the different electrode geometries and electrical configuration of SDBD plasma actuator. (a) and (e) Standard linear, (b) and (f) circular serpentine, (c) and (g) spanwise array, and (d) and (h) square serpentine SDBD actuator designs based on the shape of the line of actuation [13] (continuous black solid line). The arrows indicate the actuator forcing direction which is normal to the line of actuation. Reproduced from [13]. © IOP Publishing Ltd. All rights reserved.

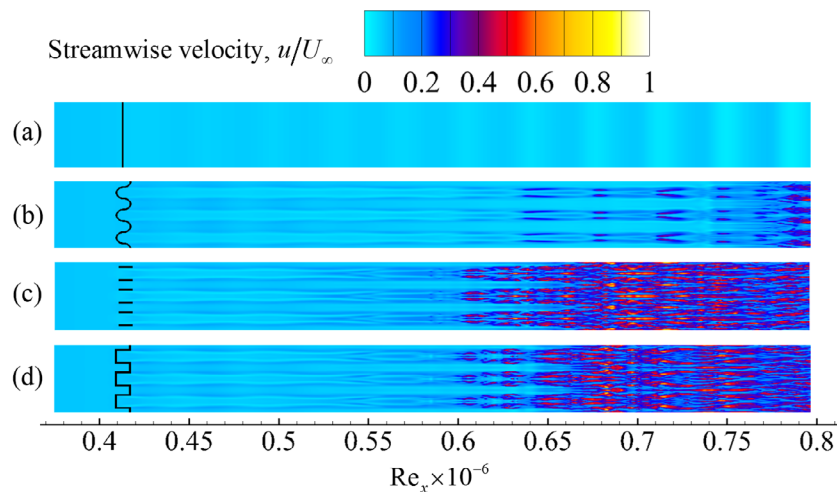


Figure 4. Normalized streamwise velocity contours depicting streaklines at $y/\delta^* = 0.2$ plane for (a) standard linear, (b) circular serpentine, (c) spanwise array, and (d) square serpentine SDBD actuator. The domain is duplicated three times in the spanwise direction. The x -axis label values have been multiplied by the number adjacent to the axis title.

wave transition scenarios [13, 42]. Except for the linear actuator, the streak pattern exhibited by all the actuators are very similar in nature. However, due to the difference in strength of streamwise vortices generated, the transition location varies. The similarity in vortical structures can be seen in the normalized Q -criterion (positive second scalar invariant of ∇u multiplied by δ_i^2/U_∞^2) iso-surface depicted in figure 5. The

spanwise and square actuators do not show large differences in the transitional region. However, around $Re_x = 6 \times 10^5$ the vortical structures generated by the spanwise actuator are more spread out in the spanwise direction. This location corresponds to the beginning of the later stages of transition for both square serpentine and spanwise actuators. Beyond this point the ‘X’ shaped structures formed due to the lambda vortices

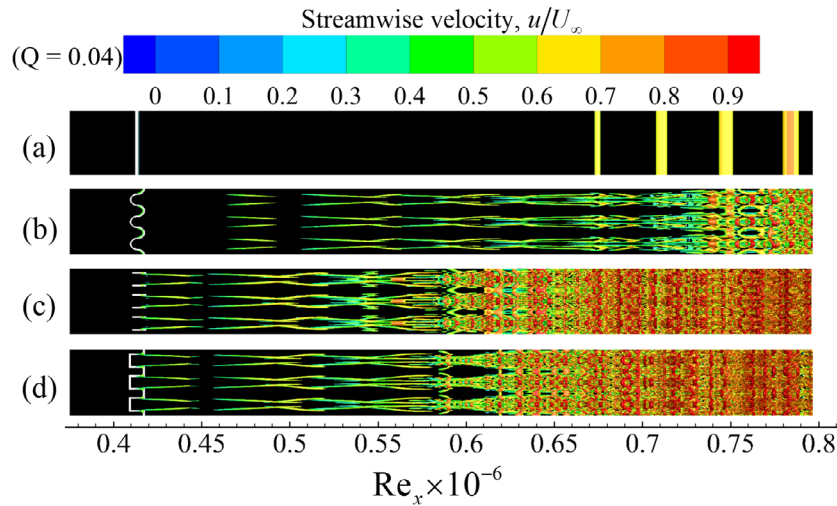


Figure 5. Top view of the instantaneous normalized Q -criterion ($Q = 0.04$) iso-surface colored with normalized streamwise velocity for (a) standard linear, (b) circular serpentine, (c) spanwise array, and (d) square serpentine SDBD actuator.

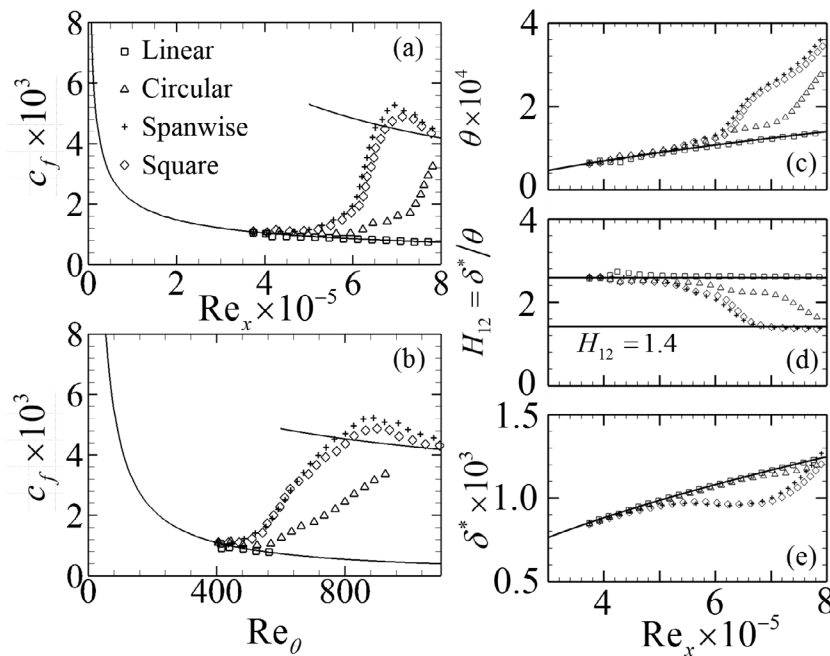


Figure 6. Variation of mean and integral quantities along the plate. Skin friction coefficient variation with Reynolds number based on (a) streamwise location and (b) momentum thickness [13] (The bottom solid line represents Blasius laminar skin friction coefficient and the top solid line represents turbulent skin friction obtained from data fit given by Schlatter and Örlü [38]). Variation of (c) momentum thickness, (d) shape factor, and (e) displacement thickness with Reynolds number based on streamwise location. Reproduced from [13]. © IOP Publishing Ltd. All rights reserved.

disappear and the turbulent structures start spreading in the spanwise direction by increasing the spanwise wavenumber of the turbulent structures. Similar behavior is observed for the circular actuator at $Re_x = 7 \times 10^5$. It should be noted that this location will also depend on the actuator forcing amplitude and frequency as discussed in the later sections.

Although the circular actuator does not transition to fully developed turbulence, it demonstrates the later stages of transition as it deviates from the laminar profile. This is evident from the skin friction plots and boundary layer integral parameters shown in figure 6. Skin friction for the linear actuator follows the Blasius profile throughout the domain. To determine the transition location it is assumed that the

flow becomes fully developed turbulent when shape factor $H_{12} = \delta^*/\theta$ (δ^* is the displacement thickness and θ is the momentum thickness) reaches 1.4 [41]. There is only a 1% difference in transition location between the spanwise and square actuator. This is because square serpentine actuator has additional streamwise directed forcing compared to the spanwise actuator. The streamwise forcing by linear plasma actuators are known to damp fluctuations [20, 43, 44]. This streamwise forcing part reduces the strength of the structures (streamwise vortices) generated by the spanwise forcing part of the square actuator. This can be observed in the near wall variation of the normalized wall-normal and spanwise RMS fluctuations at the actuator center location $Re_x = 4.13 \times 10^5$ ($Re_\theta = 430$)

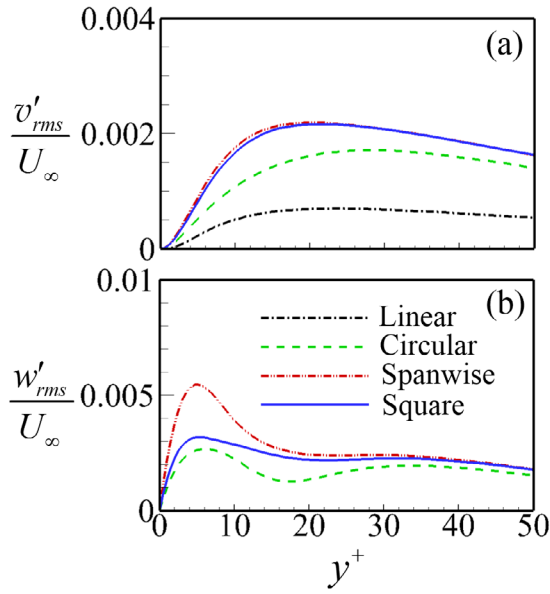


Figure 7. Variation of normalized RMS fluctuations in the near wall region for (a) wall-normal fluctuations and (b) spanwise fluctuations at $Re_x = 4.13 \times 10^5$ ($Re_\theta = 430$).

shown in figure 7. The wall-normal fluctuations are almost the same for the square and spanwise actuator. However, the strong streamwise forcing component reduces the spanwise oscillations for the square actuator and makes them comparable to the circular actuator.

The variation of fluctuation components in the wall-normal direction in the transitional region corresponding to $Re_\theta = 550$ is depicted in figure 8. This location approximately corresponds to the beginning of the later stages of transition where the skin friction quickly jumps to reach turbulent skin friction values. For spanwise and square actuator this location is $Re_x \approx 6 \times 10^5$ while for circular actuator it is $Re_x \approx 7.75 \times 10^5$. Since the linear actuator does not transition to turbulence, $Re_\theta = 550$ is the largest momentum Reynolds number achieved in the simulation. The wall-scaled RMS streamwise velocity fluctuations $u'_{rms}+$ shown in figure 8(a) has similar trend for circular, spanwise and square actuator, while the linear actuator follows the transition similar to the TS wave transition with two peaks [36, 43] in the fluctuation profile. The circular, spanwise, and square actuators show a subharmonic mode transition profile [36, 41]. The spanwise actuator has the highest amplitude fluctuations in all directions at $Re_\theta = 550$. This behavior is observed throughout the transitional region.

In figure 9 the comparison of different excited Fourier components of the normalized streamwise fluctuations by the linear, circular and square actuators are depicted. This analysis has not been conducted for the spanwise actuator since it has similar characteristics to the square actuator. The plots are constructed using twenty-one x -planes in the transitional region. Discrete Fourier transform of the fluctuations in an x -plane, provides the maximum energy component for a specific spanwise mode β . The variation in time of this particular β mode provides the frequency ω . The combination (ω, β) is

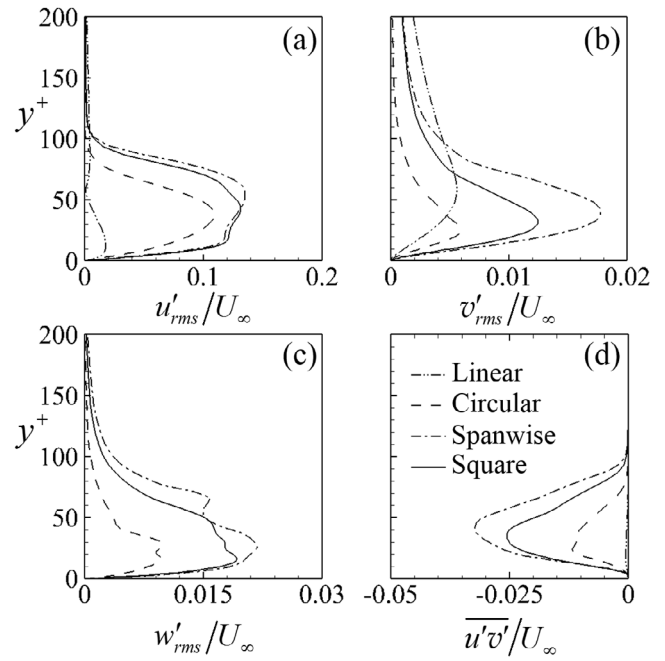


Figure 8. Variation of normalized (a) streamwise, (b) wall-normal, and (c) spanwise RMS fluctuations, and (d) Reynolds shear stress at $Re_\theta = 550$ with viscous wall units.

normalized with the actuator frequency $2\omega_0$ and wavenumber $2\pi/\lambda$ respectively. In figure 9 only the most energetic modes which are comparable in amplitude are shown.

The oblique mode which corresponds to the (1, 1)-mode is only present for the circular and square actuator. This mode has the second highest fluctuation amplitude near the actuator with (0, 1)-mode begin the highest. For the linear actuator, the mean (0, 0)-mode has the highest energy and the (2, 0)-mode has a higher energy than the (1, 0)-mode. Since the linear actuator has no spanwise variation, higher wavenumber modes are not generated. The circular and square serpentine actuators have similar amplitude for the (0, 1) and (1, 1)-modes near the actuator ($Re_x < 4.5 \times 10^5$), while the (0, 0) and (0, 2)-modes have almost twice the amplitude for the square actuator in comparison to the circular actuator. The earlier transition associated with the square actuator is mainly due to distribution of energy from the (0, 1)-mode to the (0, 2)-mode causing more turbulent production due to increase in spanwise wavenumber of the flow structures. This can be seen at $Re_x \approx 5.3 \times 10^5$ in figure 9(c) where fluctuation amplitude in (0, 2)-mode becomes higher than that of the (0, 1)-mode. The behavior at $Re_x \approx 5.3 \times 10^5$ for the square actuator can be associated with the starting phases of the subharmonic streak breakdown observed in figure 4. For the circular actuator in figure 9(b) the amplitude of (0, 2)-mode becomes higher than (0,1)-mode further downstream and based on the streak breakdown would be around $Re_x \approx 6 \times 10^5$. This difference in breakdown location between square and circular serpentine actuators leads to a delayed transition to turbulence. Therefore, altering the geometry of the actuator from circular to square impacts the mean and higher wavenumber modes promoting faster

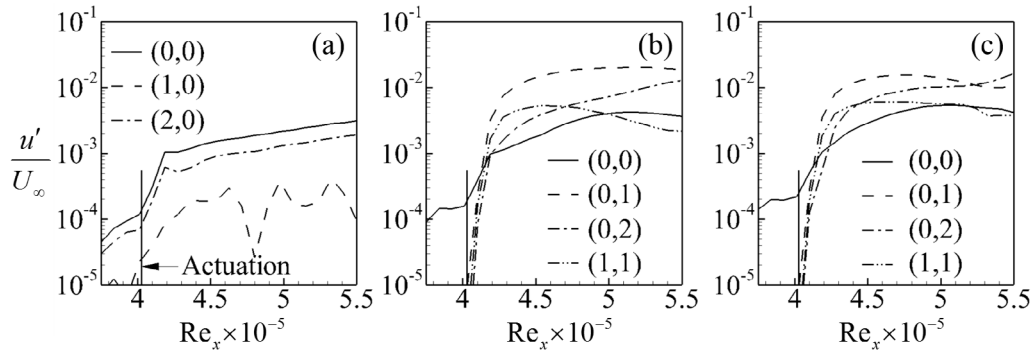


Figure 9. Variation of different Fourier components (ω, β) of normalized streamwise velocity fluctuations for (a) linear, (b) circular, and (c) square actuator.

transition while keeping the energy in the initial oblique wave similar.

In order to understand the growth of the RMS fluctuations, a growth parameter A_ψ is defined by equation (2).

$$A_\psi(x) = \int_0^{L_y} \overline{\psi(x, y)} dy. \quad (2)$$

In equation (2) L_y is the wall-normal domain size and $\overline{\psi(x, y)}$ is the time and space ensemble averaged variable for which the growth is being evaluated, for example, wall-scaled RMS streamwise velocity fluctuations u'_{rms} . The streamwise growth parameter plotted in figure 10(a) shows similar amplitude for circular, spanwise, and square actuator. However, the linear actuator has an order of magnitude lower growth parameter. This is due to the formation of lifted lambda structures [13] generated by the serpentine and spanwise actuators which causes faster growth [29] in comparison to the 2D structures generated by the linear actuator. The growth of the fluctuations changes slope at $Re_x \approx 6 \times 10^5$ for the square and spanwise actuator and at $Re_x \approx 7 \times 10^5$ for the circular actuator due to the onset of highly nonlinear structures with higher spanwise wavenumber. The local drop in streamwise growth parameter value at this transition location is due to a rapid increase in the friction velocity (used to normalize the fluctuations), while the streamwise fluctuation gradually increases. However, this drop does not occur in the wall-normal and spanwise fluctuations shown in figures 10(b) and (c) because these fluctuations rapidly increase at this location. The growth of the fluctuations in the wall-normal and spanwise direction are similar for all the actuators for $Re_x < 6 \times 10^5$. However, they have slightly different slopes (rate of growth, dA/dx) causing differences in transition location. Once the flow becomes fully developed turbulent ($Re_x \approx 6.8 \times 10^5$), all the growth parameters overlap for the square and spanwise actuator. The Reynolds shear stress growth parameter depicted in figure 10(d) shows similar trends as the wall-normal growth parameter due to its strong dependency on the wall normal fluctuations.

For the spanwise actuator, the line of actuation has the same total length (L_z) as the linear actuator while the square actuator has twice of that length ($2L_z$). This implies that less power will be dumped into the plasma formed along the line of actuation for the spanwise actuator. Therefore, even though the instantaneous structures and mean profiles for the

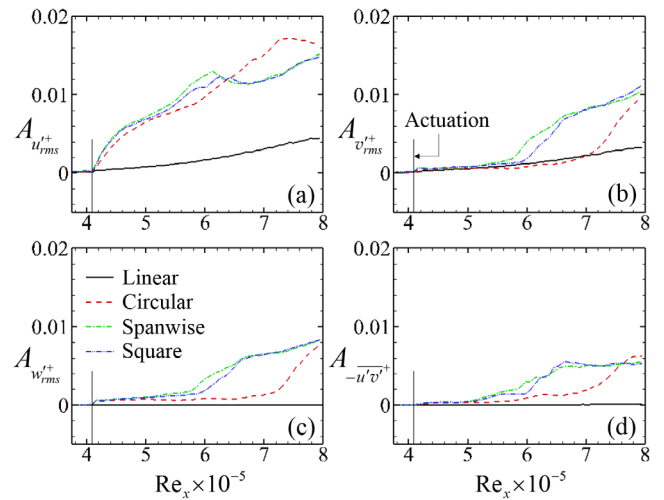


Figure 10. Growth of fluctuations normalized with wall parameters for different actuator geometries. Growth parameter for (a) streamwise, (b) wall-normal, (c) spanwise fluctuations and (d) Reynolds shear stress.

spanwise and square actuator are similar in nature, the best design for promoting turbulence for the same amplitude and frequency of actuation is the spanwise actuator. However, the total power consumption by the actuator depends on a lot of factors [45] which are difficult to analyze numerically, and experiments need to be conducted to observe whether the total electrical power consumed outweighs the benefit in altering the geometry for promoting turbulence.

3.2. Effect of frequency

Three different frequencies were investigated for the unsteady actuator forcing along with a case where the forcing was kept constant in time. The ω_0 in equation (1) is set to 500 Hz, 1 kHz, and 2 kHz for the unsteady cases and the steady forcing was achieved by setting $|\sin(\omega_0 t)| = 1$ in equation (1). It should be noted that the absolute value of sine wave makes the actual frequency of perturbation $2\omega_0$ instead of ω_0 . These frequencies are chosen because they are typical for an SDBD actuator. The velocity ratio γ is set to 0.1 for all the cases. The Strouhal number $St = 2\omega_0 \delta_i / U_\infty$ (ω_0 in rad s^{-1}) for 500 Hz, 1 kHz, and 2 kHz are 0.292, 0.584, and 1.168 respectively. If similar results are needed at different freestream

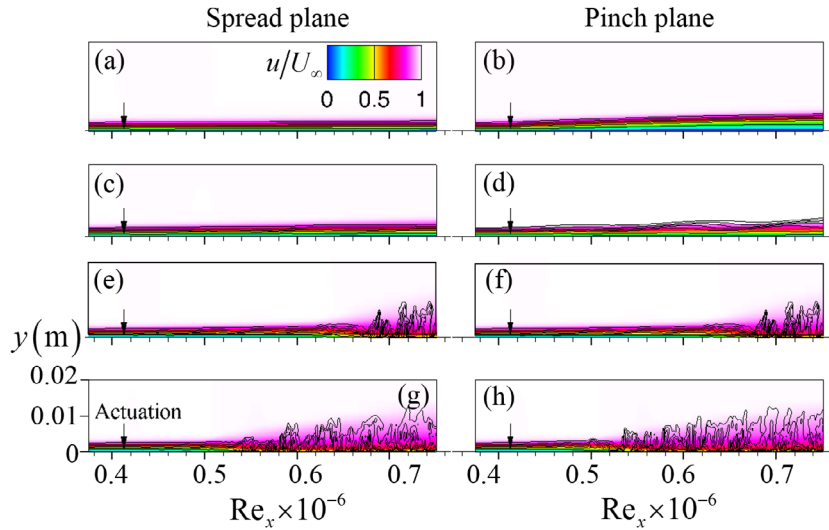


Figure 11. Normalized instantaneous velocity magnitude contour lines overlaid on normalized mean streamwise velocity for (a) and (b) steady forcing, (c) and (d) 500 Hz, (e) and (f) 1 kHz and (g) and (h) 2 kHz signal cases for the pinch (mid z -plane) and spread plane (boundary z -plane) of the square serpentine actuator ($\gamma = 0.1$). The contour lines are varying from 0 to 1 with 11 equally spaced divisions.

velocities non-dimensional parameters such as Strouhal number and velocity ratio should remain same [13].

The contours lines of freestream normalized velocity magnitude are depicted in figure 11. The pinch planes have thicker boundary layer as well as earlier transition compared to the spread planes. The continuous and 500 Hz cases do not transition to turbulence in the chosen domain. The transition occurs earlier for higher frequencies since they have lower critical Reynolds number based on the neutral stability curve [46]. The slanted structures observed in the contour lines in figures 11(d) and (f) are regions of high shear which breakdown via Kelvin Helmholtz free shear layer instability mechanism [47]. This is also a characteristic of oblique wave transition and has been observed in numerical studies [48].

For the different frequencies, the growth parameter is plotted in figure 12. The streamwise fluctuation growth parameter for the 500 Hz case has similar magnitude and slopes compared to the 1 kHz and 2 kHz cases as shown in figure 12(a). However, the wall-normal and spanwise fluctuation growth parameters show a steady decrease in growth for the 500 Hz case after the initial jump at the actuator location. This behavior shows that although the perturbations added by the actuator are 3D, the growth becomes purely 1D (only in streamwise direction) in nature for the 500 Hz and therefore is not efficient in controlling transition. This is unlike the 2D nature of the growth parameter for the linear actuator (see figure 10), where there is a growth in both streamwise and wall-normal fluctuations. The second jump observed in the growth parameter after the initial jump at the actuator location indicates final stages of transition.

3.3. Effect of perturbation amplitude

The perturbation amplitude A , in equation (1) was varied such that γ values correspond to 0.05, 0.1, and 0.14. For $\gamma = 0.05$ the flow does not reach fully developed turbulence in the chosen domain. In figure 13 it can be seen that the quasi-streamwise vortical structures for $\gamma = 0.05$ decay in

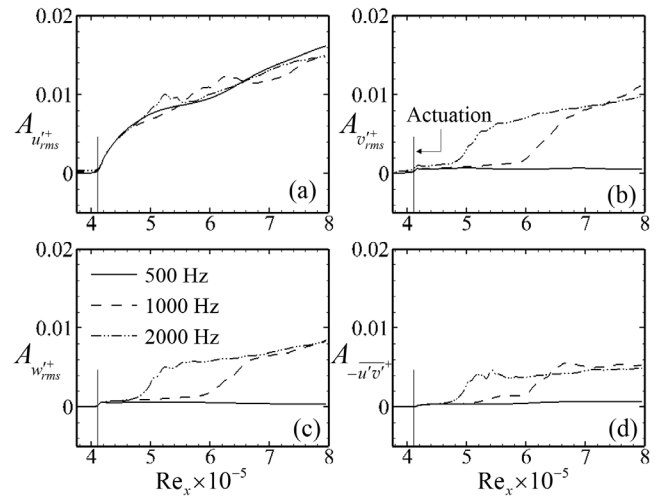


Figure 12. Growth of fluctuations normalized with wall parameters for square serpentine actuator ($\gamma = 0.1$) at different actuation frequencies. Growth parameter for (a) streamwise, (b) wall-normal, (c) spanwise RMS fluctuations and (d) Reynolds shear stress.

size and strength, downstream of the actuator, compared to the $\gamma = 0.1$ and 0.14 cases. The lambda shaped structures for the $\gamma = 0.05$ case do not create the subharmonic structures [13] (appearing in between two lambda structures) resulting in a longer transitional region. The wall pressure contours become almost 2D in nature after $Re_x \approx 6 \times 10^5$ for $\gamma = 0.05$. However, the globular structures observed downstream in figure 13(a) have the same wavenumber as the actuator and the same frequency (based on how the structures repeat along the streamwise direction), indicating the oblique mode has not dissipated. Although the higher amplitude case turbulizes faster than the lower amplitude cases, the input power required to achieve higher amplitude is also higher. However, the transition location can be advanced by 14% (2 kHz case) by increasing the amplitude by 4%, which suggests that an optimal amplitude exists to achieve an efficient flow control authority.

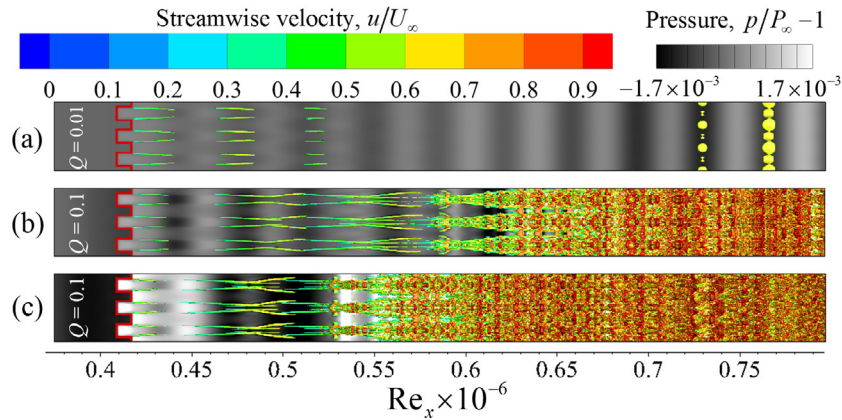


Figure 13. Top view of the instantaneous normalized Q -criterion iso-surface colored with normalized streamwise velocity for (a) $\gamma = 0.05$, (b) $\gamma = 0.1$ and (c) $\gamma = 0.14$. The normalized pressure contours at the wall are also depicted.

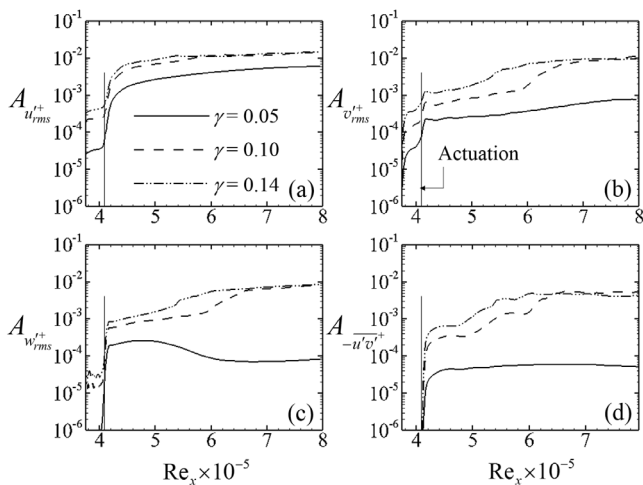


Figure 14. Growth of fluctuations normalized with wall parameters for the square serpentine actuator at different actuation amplitudes. Growth parameter for (a) streamwise, (b) wall-normal, (c) spanwise fluctuations and (d) Reynolds stress.

The variation of growth parameter for the streamwise and wall-normal fluctuations depicted in figure 14 shows that the growth rates are similar for all the velocity ratios. All the growth parameters for $\gamma = 0.1$ and $\gamma = 0.14$ converge at $Re_x \approx 7 \times 10^5$ since the flow here is fully turbulent for both the cases. After the initial increase in spanwise fluctuation at the actuator location, the growth parameter for $\gamma = 0.05$ reaches a maximum around $Re_x = 5 \times 10^5$ and then starts dropping until $Re_x = 6 \times 10^5$. Finally, it shows a gradual increase as new structures develop at a downstream location (see figure 13).

3.4. Effect of actuator heating

Three temperatures were tested with the actuator temperature T_A shown in figure 15 at 273 K, 323 K, and 373 K. The heating element shown as the black region, is applied as a boundary condition only in the pinch location. The temperature is uniform across the square heating element and it spans a wall-scaled distance of 252 units in streamwise and spanwise direction with the center coinciding with the pinch region

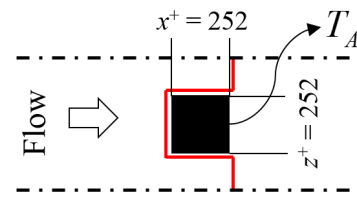


Figure 15. Schematic of the heating element applied at the pinch location of the actuator.

center. It should be noted that this is an approximate representation of the temperature distribution due to plasma formation.

Thermal heating by the actuator causes only local effects for the temperatures and flow regime tested. At the later stages of transition, the structures have different behavior based on temperature, as shown in figure 16. Adding heat lifts the hairpin structures formed at the later stages of transition further away from the wall. The vortical structures are almost indistinguishable up to $Re_x = 5.8 \times 10^5$ and then the differences start appearing. Since the hairpin structures are more lifted at higher temperatures, they tend to break down faster. It should be noted that since the flow regime is weakly compressible, the temperature effects might not be affecting the flow in the transitional region where the temperature effects have not amplified enough to be observed. Wall heating is known to significantly impact the streamwise vortical structures as well as flow instability [49, 50]. Kral and Fasel [49] studied a range of temperatures (294 K–305 K) to control transitional flow. Their non-uniform wall heating (power law variation of temperature along the streamwise direction) showed a significant reduction in growth of disturbances due to variation in wall temperature. The differences in disturbance amplitudes due to temperature were minor at the beginning of the plate and increased downstream. This is qualitatively similar to what is observed here, wherein, the discernible variations due to temperature arise only at a downstream location. Lee *et al* [50] also studied wall heating (303 K–372 K) for a fully developed turbulent boundary layer and showed 26% reduction in skin friction. However, the current study involves localized heating and the impact of heating on the flow field is not as significant as observed by Kral and Fasel [49] and Lee *et al* [50] where the entire plate was heated. The effect of localized unsteady heating was observed

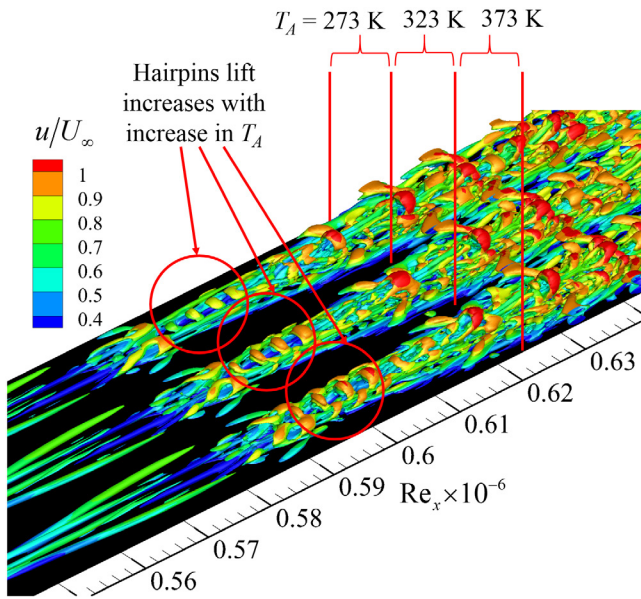


Figure 16. Instantaneous normalized Q -criterion for a square serpentine actuator for different heating element temperatures at later stages of transition. The regions between the vertical red lines mark the region for each case.

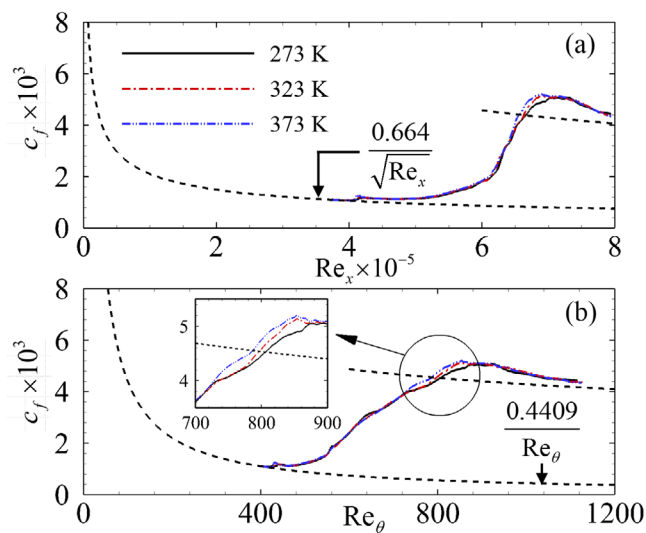


Figure 17. Variation of skin friction at different heating element temperatures with (a) Re_x and (b) Re_θ .

by Yan and Gaitonde [51], where it created localized shocks which interacted with the boundary layer. Since they studied supersonic flow ($M = 1.5$), temperature effects (660 K) were significant and caused large growth in disturbances. The NPD actuators [5, 6] also create localized shocks for flow control. These actuators can reach mean temperature differences up to 400 K [52] for a 50 ns pulse voltage signal. However, the current temperatures studied are kept steady and are not high enough to generate shock waves.

To assess the impact of the heating element, mean flow properties are also investigated. The large reduction in skin friction observed by Lee *et al* [50] was not observed here (see figure 17). This was mainly because they had uniform wall heating whereas the current study uses localized wall heating where only a small amount of thermal

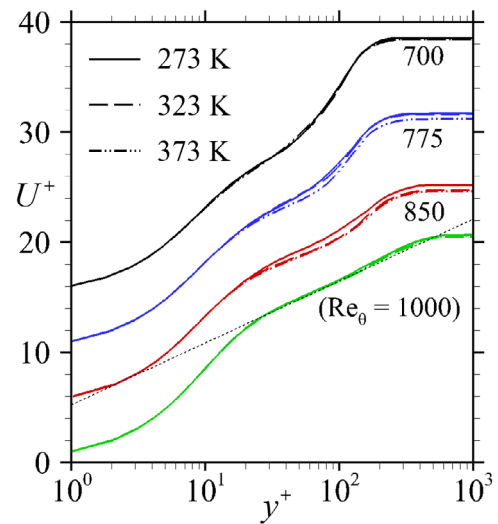


Figure 18. Variation of mean velocity profiles for different heating element temperatures and Reynolds numbers. Variation of wall-scaled mean velocity (velocities are successively shifted by 5 units, with the green curves at the right scale) with inner coordinates.

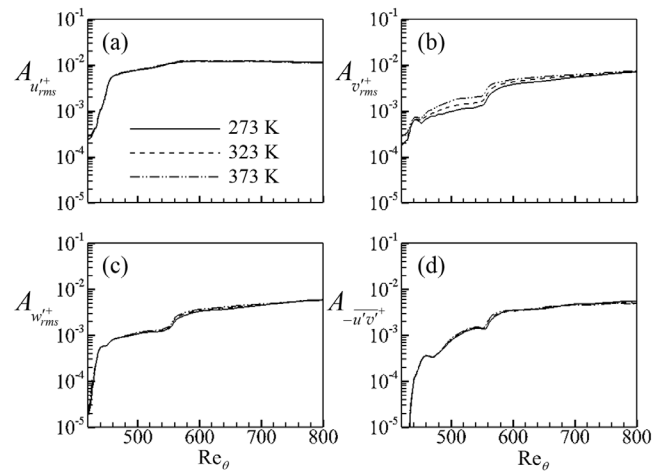


Figure 19. Variation of wall-scaled RMS fluctuations and Reynolds shear stress growth parameter with Reynolds number for different heating element temperatures. Growth parameter of (a) streamwise, (b) wall-normal and (c) spanwise RMS fluctuations and (d) Reynolds shear stress.

energy is being added. The impact on the mean skin friction profile is mainly in the later stages of transition ($Re_\theta = 750 - 900$ or $Re_x = 6.5 \times 10^5 - 7.2 \times 10^5$). The mean velocity profiles depicted in figure 18 do not show any significant differences at $Re_\theta = 700$ as well as in the fully developed turbulent region ($Re_\theta = 1000$). The variations due to heating are observed in the log layer and wake region due to the differences in friction velocity at $Re_\theta = 775$ and 850 . Since this difference is over a small streamwise region, the impact on the overall flow remains insignificant.

The growth parameter in figure 19 shows insignificant variation due to temperature, except for the wall-normal fluctuation growth. This effect also confirms the similarity in structures and the behavior of more lifted hairpin structures observed in figure 16. Therefore, the impact of actuator heating is minimal for the temperatures studied.

4. Conclusion

A detailed numerical analysis of various actuator control parameters has been conducted using wall resolved ILES to investigate their impact on the instantaneous structures and mean flow properties for a zero-pressure gradient laminar boundary layer flow over a flat plate. This study provides a thorough analysis of the effects of actuator electrode geometry on the transition mechanism. The standard linear actuator follows the Tollmien–Schlichting wave transition mechanism based on the flow structures and velocity fluctuation profile observed. The circular serpentine, square serpentine and spanwise array actuators have similar flow structure in the transitional region which corresponds to an oblique wave transition scenario. The spanwise and square actuators have almost identical flow structures with small variations in the magnitude of mean and instantaneous flow variables. The streaks generated by the serpentine and spanwise array actuators break down via subharmonic sinuous mode. Based on the energy content in different frequency-wavenumber modes, the circular and square serpentine show similar energy content in the oblique wave mode, while the higher wavenumber mode has almost twice the energy for the square actuator in comparison to the circular actuator. The growth rate of the disturbances varies based on the actuator geometry and the spanwise actuator shows the highest disturbance growth. The square actuator and spanwise actuator have small differences in the transition location ($\sim 1\%$) due to small differences in their growth of disturbances. The individual growth rates will change due to location of actuator forcing [38] and need to be further investigated.

For the square serpentine actuator design, the frequency of actuation can significantly alter the transition location for the same actuation amplitude. Higher frequencies with same amplitude and geometry of actuation promote faster transition to turbulence. However, actuation below $St = 0.292$ leads to the growth of only streamwise disturbances, while the wall-normal and spanwise disturbances decay with increase in streamwise Reynolds number, causing the transition not to occur in the chosen domain. For $\gamma = 0.05$, the flow does not transition in the chosen domain, but the disturbances grow as the streamwise Reynolds number increases. For $\gamma = 0.05$ the lambda structures generated by the actuator decay downstream, but the wavy streak pattern is present. Since the domain is not long enough to observe the full transition, the transition mechanism might change further downstream. However, the actuator does generate oblique wave (downstream of the actuator) at this velocity ratio since there are downstream globular structures which have the same wavenumber as the actuator and occur at intervals same as the actuation frequency. It should be noted that there would be a threshold γ value below which the actuator will no longer show oblique wave transition (point where fluctuations show modal growth instead of nonmodal growth observed in oblique wave transition) and the instabilities will grow spatially based on the most unstable mode generated by the actuator. When the amplitude of actuation is increased from $\gamma = 0.1$ to $\gamma = 0.14$ the transition gets advanced by 14%. It should be noted that these values are dependent of the actuator design. The perturbations due to

the forcing for $\gamma > 0.14$ were too high for transitional flow and were therefore, not investigated. This shows that for small changes in the amplitude of actuation, large differences in transition location can be achieved. Therefore, an optimal combination of frequency and amplitude of actuation exists, which can result in maximum flow control authority.

The effect of thermal heating by the square actuator was investigated for a temperature range of 273 K–373 K using a localized steady heating element. The impact of temperature was found only in the vicinity of the square actuator and in the nonlinear regions of the later stages of transition. The maximum impact of the square actuator heating is observed in the wall normal fluctuations, which causes the flow structures (hairpins) to be more lifted in the nonlinear region. However, significant differences on the overall transition process are not observed.

Acknowledgment

This work was partially supported by AFOSR grant FA9550-15-1-0424 monitored by Drs R Ponnappan and Douglas Smith.

ORCID iDs

Arnob Das Gupta  <https://orcid.org/0000-0002-6978-7791>
Subrata Roy  <https://orcid.org/0000-0002-2316-0854>

References

- [1] Wang J J, Choi K S, Feng L H, Jukes T N and Whalley R D 2013 Recent developments in DBD plasma flow control *Prog. Aerosp. Sci.* **62** 52–78
- [2] Reece J R 1995 *Industrial Plasma Engineering: Volume 1-Principles* (Boca Raton, FL: CRC Press) (<https://doi.org/10.1201/9781420050868>)
- [3] Roth J R, Sherman D M and Wilkinson S P 2000 Electrohydrodynamic flow control with a glow discharge surface plasma *AIAA J.* **38** 1166–72
- [4] Corke T C, Enloe C L and Wilkinson S P 2010 Dielectric barrier discharge plasma actuators for flow control *Ann. Rev. Fluid Mech.* **42** 505–29
- [5] Roupasov D V, Nikipelov A A, Nudnova M M and Starikovskii A Y 2009 Flow separation control by plasma actuator with nanosecond pulsed periodic discharge *AIAA J.* **47** 168–85
- [6] Correale G, Michelis T, Ragni D, Kotsonis M and Scarano F 2014 Nanosecond-pulsed plasma actuation in quiescent air and laminar boundary layer *J. Phys. D: Appl. Phys.* **47** 105201
- [7] Moreau E, Louste C and Touchard G 2008 Electric wind induced by sliding discharge in air at atmospheric pressure *J. Electrostat.* **66** 107–14
- [8] Sosa R, Arnaud E, Memin E and Artana G 2009 Study of the flow induced by a sliding discharge *IEEE Trans. Dielectr. Electr. Insul.* **16** 305–11
- [9] Roy S and Wang C C 2008 Bulk flow modification with horseshoe and serpentine plasma actuators *J. Phys. D: Appl. Phys.* **42** 032004
- [10] Durscher R J and Roy S 2012 Three-dimensional flow measurements induced from serpentine plasma actuators in quiescent air *J. Phys. D: Appl. Phys.* **45** 035202

- [11] Riherd M and Roy S 2013 Serpentine geometry plasma actuators for flow control *J. Appl. Phys.* **114** 083303
- [12] Wang L, Wong C W, Lu Z, Wu Z and Zhou Y 2017 Novel sawtooth dielectric barrier discharge plasma actuator for flow separation control *AIAA J.* **55** 1405–16
- [13] Gupta A D and Roy S 2017 Three-dimensional plasma actuation for faster transition to turbulence *J. Phys. D: Appl. Phys.* **50** 425201
- [14] Jousot R, Leroy A, Weber R, Rabat H, Loyer S and Hong D 2013 Plasma morphology and induced airflow characterization of a DBD actuator with serrated electrode *J. Phys. D: Appl. Phys.* **46** 125204
- [15] Santhanakrishnan A and Jacob J D 2007 Flow Control with plasma synthetic jet actuators *J. Phys. D: Appl. Phys.* **40** 637–51
- [16] Caruana D, Barricau P and Gleyzes C 2013 Separation control with plasma synthetic jet actuators *Int. J. Aerodyn.* **3** 71–83
- [17] Jousot R, Weber R, Leroy A and Hong D 2013 Transition control using a single plasma actuator *Int. J. Aerodyn.* **3** 26–46
- [18] Grundmann S and Tropea C 2007 Experimental transition delay using glow-discharge plasma actuators *Exp. Fluids* **42** 653–7
- [19] Simon B, Schnabel P and Grundmann S 2016 IR measurements for quantification of laminar boundary layer stabilization with dbd plasma actuators *New Results in Numerical and Experimental Fluid Mechanics X* (Berlin: Springer) pp 269–78
- [20] Riherd M and Roy S 2014 Stabilization of boundary layer streaks by plasma actuators *J. Phys. D: Appl. Phys.* **47** 125203
- [21] Porter C, McLaughlin T, Enloe C L, Font G, Roney J and Baughn J W 2007 Boundary layer control using a DBD plasma actuator *45th AIAA Aerospace Sciences Meeting and Exhibit (Reno, NV)* (<https://doi.org/10.2514/6.2007-786>)
- [22] Seraudie A, Aubert E, Naudé N and Cambonne J 2006 Effect of plasma actuators on a flat plate laminar boundary layer in subsonic conditions *3rd AIAA Flow Control Conf. (San Francisco, CA)*
- [23] Bolitho M and Jacob J 2008 Thrust vectoring flow control using plasma synthetic Jet Actuators *46th AIAA Aerospace Sciences Meeting and Exhibit (Reno, Nevada)* (<https://doi.org/10.2514/6.2008-1368>)
- [24] Dorr P C and Kloker M J 2017 Crossflow transition control by upstream flow deformation using plasma actuators *J. Appl. Phys.* **121** 063303
- [25] Huang J, Corke T C and Thomas F O 2006 Unsteady plasma actuators for separation control of low-pressure turbine blades *AIAA J.* **44** 1477–87
- [26] Visbal M R, Gaitonde D V and Roy S 2006 Control of transitional and turbulent flows using plasma-based actuators *36th AIAA Fluid Dynamics Conf. and Exhibit (San Francisco, CA)* (<https://doi.org/10.2514/6.2006-3230>)
- [27] Sekimoto S, Nonomura T and Fujii K 2017 Burst-mode frequency effects of dielectric barrier discharge plasma actuator for separation control *AIAA J.* **55** 1385–92
- [28] Bénard N, Note P, Caron M and Moreau E 2017 Highly time-resolved investigation of the electric wind caused by surface DBD at various ac frequencies *J. Electrostat.* **88** 41–8
- [29] Andersson P, Berggren M and Henningson D S 1999 Optimal disturbances and bypass transition in boundary layers *Phys. Fluids* **11** 134–50
- [30] Kendall J M 1985 Experimental study of disturbances produced in a pre-transitional laminar boundary layer by weak freestream turbulence *18th Fluid Dynamics and Plasmadynamics and Lasers Conf. (Cincinnati, OH)* (<https://doi.org/10.2514/6.1985-1695>)
- [31] Roy S, Zhao P, Gupta A D and Soni J 2016 Dielectric Barrier Discharge actuator for vehicle drag reduction at highway speeds *AIP Adv.* **6** 025322
- [32] Jousot R, Boucinha V, Weber-Rozenbaum R, Rabat H, Leroy-Chesneau A and Hong D 2010 Thermal characterization of a DBD plasma actuator: dielectric temperature measurements using infrared thermography *40th Fluid Dynamics Conference and Exhibit (Chicago, IL)* (<https://doi.org/10.2514/6.2010-5102>)
- [33] Durscher R and Roy S 2011 Aerogel and ferroelectric dielectric materials for plasma actuators *J. Phys. D: Appl. Phys.* **45** 012001
- [34] Choi H and Moin P 1994 Effects of the computational time step on numerical solutions of turbulent flow *J. Comp. Phys.* **113** 1–4
- [35] Wu X and Moin P 2009 Direct numerical simulation of turbulence in a nominally zero-pressure-gradient flat-plate boundary layer *J. Fluid Mech.* **630** 5–41
- [36] Sayadi T, Hamman C W and Moin P 2013 Direct numerical simulation of complete H-type and K-type transitions with implications for the dynamics of turbulent boundary layers *J. Fluid Mech.* **724** 480–509
- [37] Singh K P and Roy S 2008 Force approximation for a plasma actuator operating in atmospheric air *J. Appl. Phys.* **103** 013305
- [38] Schlatter P and Örlü R 2012 Turbulent boundary layers at moderate Reynolds numbers: inflow length and tripping effects *J. Fluid Mech.* **710** 5–34
- [39] Israeli M and Orszag S A 1981 Approximation of radiation boundary conditions *J. Comput. Phys.* **41** 115–35
- [40] Bénard N and Moreau E 2014 Electrical and mechanical characteristics of surface AC dielectric barrier discharge plasma actuators applied to airflow control *Exp. Fluids* **55** 1846
- [41] Schlichting H and Gersten K 2017 *Boundary-Layer Theory* (Berlin: Springer)
- [42] Elofsson P A and Alfredsson P H 2000 An experimental study of oblique transition in a Blasius boundary layer flow *Euro. J. Mech. B* **19** 615–36
- [43] Riherd M and Roy S 2013 Damping Tollmien–Schlichting waves in a boundary layer using plasma actuators *J. Phys. D: Appl. Phys.* **46** 485203
- [44] Grundmann S and Tropea C 2008 Active cancellation of artificially introduced Tollmien–Schlichting waves using plasma actuators *Exp. Fluids* **44** 795–806
- [45] Roth J R and Dai X 2006 Optimization of the aerodynamic plasma actuator as an electrohydrodynamic (EHD) electrical device *44th AIAA Aerospace Sciences Meeting and Exhibit (Reno, Nevada)* (<https://doi.org/10.2514/6.2006-1203>)
- [46] Jordinson R 1970 The flat plate boundary layer. Part 1. Numerical integration of the Orr–Sommerfeld equation *J. Fluid Mech.* **43** 801–11
- [47] Lasheras J C and Choi H 1988 Three-dimensional instability of a plane free shear layer: an experimental study of the formation and evolution of streamwise vortices *J. Fluid Mech.* **189** 53–86
- [48] Berlin S, Lundbladh A and Henningson D 1994 Spatial simulations of oblique transition in a boundary layer *Phys. Fluids* **6** 1949–51
- [49] Kral L D and Fasel H F 1994 Direct numerical simulation of passive control of three-dimensional phenomena in boundary-layer transition using wall heating *J. Fluid Mech.* **264** 213–54
- [50] Lee J, Jung S Y, Sung H J and Zaki T A 2013 Effect of wall heating on turbulent boundary layers with temperature-dependent viscosity *J. Fluid Mech.* **726** 196–225
- [51] Yan H and Gaitonde D 2010 Effect of thermally induced perturbation in supersonic boundary layers *Phys. Fluids* **22** 064101
- [52] Starikovskii A Y, Nikipelov A A, Nudnova M M and Roupasov D V 2009 SDBD plasma actuator with nanosecond pulse-periodic discharge *Plasma Sources Sci. Technol.* **18** 034015